Published in final edited form as:

Nat Chem. 2020 December ; 12(12): 1123–1130. doi:10.1038/s41557-020-00554-5.

Shortwave infrared polymethine fluorophores matched to excitation lasers enable noninvasive, multicolor *in vivo* imaging in real time

Emily D. Cosco[#,^], **Anthony L. Spearman**[#], **Shyam Ramakrishnan**[^], **Jakob G. P. Lingg**[^], **Mara Saccomano**[^], **Monica Pengshung**[#], **Bernardo A. Arús**[^], **Kelly C. Y. Wong**[#], **Sarah Glasl**[&], **Vasilis Ntziachristos**[&], **Martin Warmer**[^], **Ryan R. McLaughlin**[#], **Oliver T. Bruns**[^,*], **Ellen M. Sletten**[#,*]

[#] Department of Chemistry and Biochemistry, University of California, Los Angeles, Los Angeles, California, 90095, United States

[^] Helmholtz Pioneer Campus, Helmholtz Zentrum München, D-85764 Neuherberg, Germany

[&] Institute of Biomedical Imaging, Helmholtz Zentrum München, D-85764 Neuherberg, Germany

Abstract

High resolution, multiplexed experiments are a staple in cellular imaging. Analogous experiments in animals are challenging, however, due to significant scattering and autofluorescence in tissue at visible (VIS, 350–700 nm) and near-infrared (NIR, 700–1000 nm) wavelengths. Here, we enable real-time, non-invasive multicolor imaging experiments in animals through the design of optical contrast agents for the shortwave infrared (SWIR, 1000–2000 nm) region and complementary advances in imaging technologies. We developed tunable, SWIR-emissive flavylium polymethine dyes and established structure-photophysical property relationships for this class of bright SWIR contrast agents. In parallel, we designed an imaging system with variable NIR/SWIR excitation and single-channel detection, facilitating video-rate multicolor SWIR imaging for optically guided surgery and imaging of awake and moving mice with multiplexed detection. Optimized dyes matched to 980 nm and 1064 nm lasers, combined with the clinically approved indocyanine green, enabled real-time, three-color imaging with high temporal and spatial resolutions.

[*]**Corresponding authors:** Ellen Sletten, Phone: +1 (310) 825-4452, sletten@ucla.edu, Address: 607 Charles E. Young Dr. East, Los Angeles, CA 90095, Oliver Bruns, Phone: + 49 (0) 89 3187 49494, oliver.bruns@helmholtz-muenchen.de, Address: Ingolstaedter Landstraße 1, D-85764 Neuherberg, Germany.

Author Contributions

E.D.C., E.M.S. and O.T.B. designed the study. E.M.S. and O.T.B. jointly advised the study. E.D.C., A.L.S., M.P. and R.R.M performed synthesis. E.D.C. measured and analyzed photophysics. S.R. developed software and built electronics and instrumentation.; E.D.C., J.G.P.L. and M.W. built optical configurations. E.D.C., M.S., B.A.A. and S.G. performed imaging experiments. E.D.C., J.G.P.L. and B.A.A. analyzed images. K.C.Y.W. performed cell culture experiments. E.D.C., E.M.S. and O.T.B. wrote and edited the paper. E.M.S., O.T.B. and V.N. provided funding. All authors have given approval to the final version of the manuscript.

Competing interests

Material presented in this work is included in patent and patent applications US20200140404, EP3634397, and WO2018226720 with authors E.M.S and E.D.C. and PCT/EP2020065753 with authors O.T.B., E.D.C., J.G.P.L., M.W., S.R., M.S. and E.M.S.

Data availability. Image data sets, including all raw and processed imaging data generated in this work are available at BioImage Archive. All other datasets that support the findings of this study are contained within the manuscript and its Supporting Information.

Code availability. Custom computer programs used for the work are available at github.

Keywords

polymethine dyes; optical imaging; shortwave infrared; excitation multiplexing

Improvements in imaging technologies and optical probes have combined to revolutionize our ability to study cells and small organisms using fluorescence microscopy.[1,2] The tools developed for fluorescent imaging in cells can be readily applied to small model organisms such as *C. elegans, D. rerio* (zebrafish), and *Drosophila*. Translating these tools to mammals is challenging, however, as most fluorophores used in cellular imaging are excited by light in the visible (VIS, 350–700 nm) region of the electromagnetic spectrum, which exhibits low photon penetration and high background autofluorescence. For these reasons, imaging in mammals has been primarily focused on the near-infrared (NIR, 700–1000 nm) region, where there are fewer endogenous chromophores, but where light scattering remains a limitation.[3] Further, the limited wavelength range of the NIR makes multiplexed experiments challenging. Notable approaches to multicolor fluorescence imaging experiments in mice that are compatible with VIS and NIR fluorophores include 2-photon intravital microscopy methods, requiring body windows,[4,5,6,7] or endoscopy[8]. Efforts toward non-invasive, multiplexed imaging in mice have been explored with quantum dots,[9] fluorescently-labeled silica particles,[10] fluorescent proteins,[11] and SERS nanoparticles[12]. While significant advances, these approaches suffer from low spatial and temporal resolution, limiting the biological information that can be obtained.

To enable robust, real-time, multiplexed imaging in animals it is necessary to: 1) detect in a region of the electromagnetic spectrum which provides high spatial resolution; 2) establish efficient, orthogonal excitation and/or detection of bright fluorophores; and 3) rapidly detect each channel on the millisecond (ms) time scale. Here, we present a method that meets these requirements and enables whole animal, three-color imaging with high spatial and temporal resolutions. Key to this technique is the implementation of excitation-multiplexing and “color-blind” single-channel detection of low-energy shortwave infrared (SWIR, 1000–2000 nm) light emitted by bright, “excitation-matched” polymethine fluorophores (Fig. 1a).

The SWIR region is essential for multiplexed *in vivo* fluorescence imaging, as it provides superior resolution and greater tissue penetration than the NIR region[13,14] in addition to an expanded range of wavelengths allowing for multiple channels separated by at least 80 nm. [15] The optimal properties of the SWIR for *in vivo* imaging were first demonstrated with carbon nanotubes,[16] and further validated with quantum dots,[17,18] rare-earth nanomaterials, [15] and small molecules.[19,20] Combinations of these materials have been utilized to obtain multiplexed images in mice[18,21,22,23] and tissues[24] at higher spatial resolutions than the NIR. The excitation-multiplexing with single-channel SWIR detection approach reported herein addresses multicolor SWIR imaging with high temporal resolution, facilitating real-time analysis (>27 fps) of biological processes at sub-millimeter resolutions.

To facilitate rapid multicolor imaging in the SWIR region, we diverged from traditional multiplexing approaches employing a common excitation wavelength and different detection windows,[21,22,23,24,25,] or spectral unmixing[18]. These classic approaches can result in different resolutions for each channel due to dramatic changes in the contrast and resolution

that occur throughout wavelength bands of the NIR and SWIR.[14,26,27] Furthermore, fast imaging speeds can be impeded by low photon throughput in sectioned regions of the electromagnetic spectrum or by mechanical components, such as filter wheels. Instead of these approaches, we differentiate the contrast agents via excitation wavelength and employ a single SWIR detection channel. This method, referred to as excitation-multiplexing, is advantageous due to the consistent resolution achieved in all channels, high photon efficiency, and the ease of rapid collection of each frame on a single detector.[28,29] Excitation-multiplexing was initially applied to single-molecule spectroscopy methods, microscopy, and low concentration DNA-sequencing[30]. Subsequent variations on these methods have been explored[31,32], but excitation-multiplexed methods have yet to be adapted for animals. The implementation of excitation-multiplexing in the SWIR is particularly beneficial as excitation can be optimized for each fluorophore and photons can be detected over a wide range of wavelengths. These properties combine to maximize the signal obtained from SWIR contrast agents, which have inherently low quantum yields when compared to those in the VIS and NIR.[33]

To perform real-time excitation-multiplexing in animals, bright SWIR emissive contrast agents with absorption spectra compatible with common and cost-efficient laser lines are required (Fig. 1b). Polymethine dyes are opportune contrast agents for excitation multiplexing as they have characteristically narrow absorption bands with high absorption coefficients.[34] A marquee member of the polymethine dye family is indocyanine green (ICG), an FDA approved contrast agent.[35,36] While ICG has been extensively used in NIR optical imaging, in 2017, we reported that the dye can be detected readily in a SWIR imaging configuration due to the long tail of the emission spectrum.[37,38] Concurrently, we reported the first polymethine dye designed for SWIR optical imaging.[39] This dye, Flav7 (1, Fig. 1c), has both SWIR absorption and high brightness for the SWIR region. Notably, since the report of Flav7, similar strategies have been employed to utilize or design polymethine dyes for SWIR imaging.[40,41,42,43,44] Due to the ability to image both bright NIR-excitable dyes, such as ICG, as well as red-shifted SWIR-excitable polymethine dyes, such as Flav7, with an identical SWIR detection window, we envisioned that polymethine dyes with both well-separated and laser-line compatible absorption could enable efficient multicolor SWIR imaging via excitation-multiplexing. To realize this multiplexing strategy, structural modifications to Flav7 were necessary to tune the $\lambda_{max,abs}$ to match accessible laser wavelengths used for SWIR imaging. Towards this goal, we set out to fine-tune the absorption properties of flavylium polymethine dyes through heterocycle modification. This work ultimately allowed access to a set of dyes which were optimal for real-time, multicolor SWIR imaging.

Results:

Design and synthesis of flavylium heptamethine dyes. To tune the absorption properties of flavylium polymethine dyes for excitation-multiplexing, robust synthetic approaches toward flavylium heterocycles were necessary. The original report of Flav7 used a previously published[45], low-yielding, electronically-sensitive, and potentially explosive route. Thus, we developed an alternate approach relying on a key 7-substituted flavone intermediate that could be converted to the desired heterocycles by treatment with a methyl nucleophile and

dehydration (Extended Data Fig. 1).[46] Using three general routes to flavones: 1) Mentzer pyrone synthesis,[47]; 2) functionalization of 7-hydroxy flavone by Buchwald-Hartwig coupling of the corresponding triflate[48] and; 3) acylation of the commercial 7-amino flavone, we accessed a diverse set of 7-amino flavylium heterocycles (Supplementary Tables 1–3). The heptamethine dyes 1–11 were then obtained through the base-promoted reaction of each flavylium heterocycle with the relevant bis(phenylimine) polymethine chain (Supplementary Table 4, see Supplementary Note 1 for further discussion).

Photophysical characterization of flavylium heptamethine dyes. Differences in $\lambda_{max,abs}$ are essential for excitation-multiplexing. We characterized the photophysical properties of 1–11 in dichloromethane, finding that the flavylium heptamethine dyes have absorption/emission spanning the NIR to SWIR regions of the electromagnetic spectrum (Fig. 2a–d). Compared to Flav7 (1), with $\lambda_{max,\,abs}$ = 1027 nm, 9 and 10 underwent significant hypsochromic shifts. The 7-methoxy-substituted dye 10 is ~43 nm blue-shifted from Flav7 ($\lambda_{max,\,abs}$ = 984 nm), similar to the un-substituted flavylium dye 11 (IR-27[49]). Conversely, dyes 3 and 7 displayed substantial bathochromic shifts compared to Flav7. The diphenylamino-substituted 7 is ~23 nm red-shifted, while julolidine derivative 3 is red-shifted by ~35 nm ($\lambda_{max,\,abs}$ = 1061 nm). Linear and cyclic aliphatic amine substituted dyes 2, 4–6 exhibit minor red-shifts. Plotting absorption/emission wavelengths of nine dyes in the series against Hammett σ_m values[50] resulted in a strong correlation (R^2 = 0.96) (Fig. 2e, Supplementary Note 2). This increased understanding of the relationship between structure and absorption/emission wavelengths sets up opportunities for predicting fluorophore structures to match any desired excitation wavelength.

Further characterization of the panel of flavylium polymethine dyes was necessary to determine their maximum brightness (brightness(ε_λ) = $\varepsilon_\lambda \times \Phi_F$). We found that the absorption coefficients (ε) vary from ~110,000 to ~240,000 $M^{-1}cm^{-1}$, in line with high absorption cross-sections characteristic for polymethine fluorophores.[34] The fluorescence quantum yields (Φ_F, relative measurements to IR-26 = 0.05%[51,52], see Supplementary Note 3) remain rather constant, in the 0.4–0.6% range. The combined high, and relatively consistent ε and Φ_F values result in a series of bright dyes spanning from 984–1061 nm (Fig. 2d), primed for real-time, excitation multiplexing in the SWIR.

Excitation-multiplexing with flavylium SWIR dyes. For excitation-multiplexing, we are most interested in properties of the series of polymethine fluorophores when excited at 980 and 1064 nm, as these wavelengths correspond to readily available, low cost, and high power (≥ 25 W) continuous-wave (CW) lasers and allow for multiplexing with established dyes like ICG and IRDye 800CW at 785 or 808 nm. Thus, we calculated brightness(ε_λ) values for each dye using the absorbance coefficient at the relevant wavelengths. The variation in brightness when excited at the wavelength of interest vs. all other wavelengths used determines the amount of cross-talk between channels. Cross-talk reduces the contrast between channels, limiting the dynamic range. From Fig. 2f and Supplementary Fig. 1, we observe that Flav7 (1) has similar brightness when excited with 980 or 1064 nm light, and thus is poorly-suited for excitation multiplexing with these lasers. Examining Fig. 2f,

candidates emerge for excitation-multiplexed imaging, with 3 (named JuloFlav7) being superior for imaging at 1064 nm (brightness(ε_{1064}) = 1090 ± 40 $M^{-1}cm^{-1}$) and 10 (named MeOFlav7) having the advantage at 980 nm (brightness(ε_{980}) = 980 ± 20 $M^{-1}cm^{-1}$). We further analyzed the photophysics of JuloFlav7 (3) for multiplexing using the percent difference of brightness at λ = 1064 vs. λ = 980 nm as a numerical metric to predict multiplexing performance and found that JuloFlav7 (3) is predicted to have the lowest levels of cross-talk compared to existing polymethine dyes (Supplementary Fig. 2).[19,41,41] This "excitation matching" concept can be further visualized by observing the absorption profiles and excitation wavelengths on the same plot (Fig. 3a). Employing ICG, which is well-matched to the common 785 nm laser, adds a third color.

To perform excitation-multiplexing with single-channel SWIR detection using the new, bright SWIR-emissive dyes, a custom SWIR imaging configuration with three lasers and a fast InGaAs camera was constructed (Supplementary Fig. 3). With 785, 980 and 1064 nm lasers, tailored excitation could preferentially excite three fluorophores. Emission is detected in a color-blind fashion using identical filters and settings for all channels. This approach provides high-resolution images without optical aberrations arising from detection at different wavelengths (see Extended Data Figs. 2–3 and Supplementary Note 4 for multiplexing resolution effects). In addition, this method enables fast acquisition of all channels in each imaging frame by using rapidly-modulated excitation sources and identical acquisition settings in a single detector. To accomplish real-time imaging, triggers on the ms time scale are sent independently to each CW laser and the detector is programmed to collect a single frame for each sequential excitation pulse (Supplementary Note 5). While the effective frame rate of collection is slowed by a factor equal to the number of channels, video-rate acquisition was still achievable due to the well-matched, bright fluorophores.

In preparation for *in vivo* delivery of SWIR dyes, JuloFlav7 (3) and MeOFlav7 (10) were encapsulated in PEG-coated micelles to impart water solubility (Supplementary Figs. 4–5). The micelle-encapsulated dyes demonstrate low toxicities to mammalian cells (Supplementary Fig. 6). The aqueous-soluble formulations of 3 and 10 display aggregation, which decreases the concentration of emissive species present in the aqueous environment, but does not significantly alter their excitation or emission profiles (Fig. 3b–d; Supplementary Fig. 7). We verified that excitation-multiplexing proceeded in both organic and aqueous environments by imaging tubes containing ICG (left), MeOFlav7 (10, center) and JuloFlav7 (3, right) (Fig. 3e) in organic solvent (top), and micelle-encapsulations in water (middle). In each case, three successive frames collected with 785, 980, and 1064 nm lasers show high intensities in the left, center, and right samples, respectively. Merging the three frames together yields a three-color image representing one effective multiplexed frame. Because molecules absorb minimal light at energies lower than their S_0 to S_1 transition, cross-talk occurs primarily in one direction. Linear unmixing can correct for minor signal overlaps between channels as seen in Fig. 3e (bottom) and further discussed in the Figure experimental procedures in the Supplementary Information.

In vivo demonstration of multicolor SWIR imaging. Using single channel imaging, we validated that micelles containing JuloFlav7 (3) could be imaged with 8–9 ms exposure time

after intravenous (i.v.) injection through a tail vein catheter in anesthetized mice, under 1064 nm excitation and 1150–1700 nm detection (Supplementary Video 1, Extended Data Fig. 4). The high signal-to-noise-ratio (SNR) obtained at 100 frames per second (fps), the fastest SWIR imaging demonstrated to date, was encouraging and suggested that video-rate speeds would be attainable upon addition of multiple channels. Further, the “excitation-matching” strategy was validated by a ~10-fold improvement in speed compared to previously reported polymethine chromophores for imaging with 1064 nm excitation (Supplementary Fig. 2). We performed three-color imaging *in vivo* by first performing an intraperitoneal (i.p.) injection of MeOFlav7 (10), followed by i.v. injections of JuloFlav7 (3), and finally ICG (Fig. 3f, Supplementary Videos 2–3). Representative time points of the three-color video are displayed in Fig. 3g and Supplementary Fig. 8. The (bio)distribution of each dye over any position can be determined from the relative contributions of the three channels, as visualized in the single channel images. After establishing both the technology and the molecular tools for multiplexed real-time observation of function in mice, the next goal was to enhance applications of SWIR imaging.

Applications of multicolor real-time SWIR imaging. Physiological properties such as heart-rate, respiratory rate, thermoregulation, metabolism, and central nervous system function, are highly impacted by anesthesia.[53] Methods to observe animals in their natural state are necessary to study physiology, but are currently limited to telemetric sensors and electrocardiography, involving surgical implantation[54] or external contact[55], respectively. Recently, high-speed SWIR imaging has enabled contact-free monitoring of physiology in awake mice.[18] Due to frame rates which are faster than macroscopic movements in animals, the heart-rate and respiratory rate in awake animals can be quantified. In this study, we expanded this technique by observing awake, unperturbed mice in three colors. In Fig. 4a, Supplementary Fig. 9 and Supplementary Video 4, awake mouse imaging was performed 80 minutes after i.p. administration of MeOFlav7 (10) and consecutive i.v. administration of JuloFlav7 (3) and ICG. From the top-view of the moving mouse, ICG could be visualized exclusively in the liver, MeOFlav7 (10) in the abdomen, while JuloFlav7 (3) remained systemically distributed throughout the mouse. In addition to the ability to assess natural physiology, such as the awake breathing rate (Fig. 4b, quantified here at 247 breaths per minute), contact-free, these tools foreshadow more complex experiments in which the location of multiple probes could be monitored longitudinally, non-invasively, and without anesthesia.

Secondly, biodistribution of two species can be monitored in the same organs. For example, the accumulation and clearance from the liver of each probe can be observed and decoupled. We injected JuloFlav7 (3) and ICG consecutively through the tail vein and imaged the whole mouse at several time points over a one-hour period (Fig. 4c). In the duration of the experiment, the liver signal from the 1064 channel remained constant, in contrast to the 785 channel which shows depletion over time. (Fig. 4d, Supplementary Fig. 10). The fast acquisition speeds obtained via excitation multiplexing enable real-time (50 fps in two colors) feedback during necropsies and surgeries (Fig. 4e, Supplementary Video 5). The methods reported herein are not only applicable to non-invasive imaging but also in aiding surgeons in identifying essential and/or diseased structures during intraoperative procedures.[56,57]

A widely investigated use of fluorescence-guided surgery is for the lymphatic system, both to identify sentinel lymph nodes implicated in cancer[58] and to assess the structure/function of lymphatic networks in lymphovascular disorders[59]. A complementary clinical need is to safely and quickly assess vascular function.[60] With administration of ICG and JuloFlav7 (3) in the lymphatic and circulatory systems, respectively, both essential functions can be observed simultaneously. ICG was injected intradermally into the footpads and the tail. After 40 minutes, ICG had accumulated in the lymph system and the pulsating motion of the collecting lymphatic vessels could be observed (Supplementary Video 6). Subsequently, JuloFlav7 (3) was injected intravenously, immediately filling the vasculature (Figs. 5a–c, Supplementary Fig. 11, Supplementary Video 6). Image collection at 21 fps in two channels gave high spatially and temporally resolved images with separate visualization of lymph vessels from veins and arteries (Figs. 5d–e, Supplementary Fig. 12). Notably, the function of each vessel, modeled by the signal across a linear cross-section, can be observed in real-time (Fig. 5f). The ability to differentiate lymph and circulatory structures and simultaneously monitor their function has implications in non-invasive diagnostics as well as in expanding technologies for fluorescence-guided surgery

Discussion:

Despite the large set of optical tools developed for the VIS and NIR regions of the electromagnetic spectrum which enable fast, multiplexed detection in small model organisms, non-invasive, multicolor imaging in mammals with high resolution is still a significant challenge. By developing predictably tunable SWIR polymethine fluorophores, along with a triggered multi-excitation SWIR optical configuration, we demonstrated multicolor whole-animal imaging at video-rate speeds and sub-millimeter resolution. The excitation-multiplexing with single-channel SWIR detection approach presented here both minimizes challenges due to low quantum yields of SWIR fluorophores by using efficient excitation and detection, and expands the wavelengths of the electromagnetic spectrum compatible with multicolor deep-tissue imaging. Several key advances were necessary to successfully translate excitation-multiplexed imaging methods to whole animals. The ability to fine-tune the spectral properties of the fluorophores to “excitation-match” relevant lasers was accomplished by systematic functional group manipulation on a bright SWIR dye scaffold. These studies revealed predictive metrics for SWIR fluorophore absorption/emission using physical organic chemistry and produced MeOFlav7 (10) well-matched to 980 nm and JuloFlav7 (3) well-matched to 1064 nm. These dyes, along with FDA-approved ICG, enable single-channel imaging at 100 fps and two/three-color imaging at video-rate speeds (≥ 27 fps). Ultimately, we envision that “excitation-matching” will be an essential design principle for future optimization and utility of fluorophores and other light-activated probes.

The technologies open a new realm in monitoring orthogonal function in mammals, even in awake animals without restraint or implantation. Furthermore, the rapid acquisition speeds combined with the high spatial resolution at which multiplexed imaging can be performed will enable real-time information regarding the localization of tagged biomolecules, labeled structures (e.g. a tumor), and anatomical reference structures such as tissues (e.g. liver or bones) and blood and lymphatic vessels. These tools, as well as further exploration of

polymethine-based probes and development of clinical imaging systems, will enable superior surgical, diagnostic, and biomedical studies.

Methods.

Materials

Chemical reagents were purchased from Accela, Acros Organics, Alfa Aesar, Carl Roth, Fisher Scientific, Sigma-Aldrich, or TCI and used without purification unless noted otherwise. Lipids were purchased from Laysan Bio and Avanti Polar Lipids. Anhydrous and deoxygenated solvents (toluene, THF) were dispensed from a Grubb's-type Phoenix Solvent Drying System constructed by J.C. Meyer. Anhydrous solvents were prepared by drying over 4 Å molecular sieves for at least 3 days (1,4-dioxane, ethanol, *n*-butanol, *n*-pentanol) or dried with $CaCl_2$, followed by $MgSO_4$, and distilled (EtOAc). Oxygen was removed by three consecutive freeze–pump–thaw cycles in air-free glassware directly before use.

Instrumentation

Thin layer chromatography was performed using Silica Gel 60 F_{254} (EMD Millipore) plates. Flash chromatography was executed with technical grade silica gel with 60 Å pores and 40–63 μm mesh particle size (Sorbtech Technologies). Solvent was removed under reduced pressure with a Büchi Rotavapor with a Welch self-cleaning dry vacuum pump and further dried with a Welch DuoSeal pump. Bath sonication was performed using a Branson 3800 ultrasonic cleaner or an Elma S15Elmasonic. Nuclear magnetic resonance (^{1}H NMR, ^{13}C NMR, and ^{19}F NMR) spectra were taken on Bruker Avance 300, AV-400, AV-500 or AV-600 instruments and processed with MestReNova or TopSpin software. All ^{1}H NMR and ^{13}C NMR peaks are reported in ppm in reference to their respective solvent signals. ^{19}F NMR spectra are reported in ppm in reference to α,α,α-trifluorotoluene at −63.90 ppm as an external standard.[61] High resolution mass spectra (electrospray ionization (ESI)) were obtained on a Thermo Scientific Q Exactive™ Plus Hybrid Quadrupole-Orbitrap™ M with Dionex UltiMate 3000 RSLCnano System. IR spectra were obtained on a Perkin-Elmer UATR Two FT-IR spectrometer and are reported in terms of frequency of absorption (cm^{-1}). Nanomaterial size was analyzed with a Malvern Zetasizer Nano dynamic light scattering in plastic 1 cm cuvettes. Absorbance spectra were collected on a JASCO V-770 UV-Visible/NIR spectrophotometer with a 2000 nm/min scan rate after blanking with the appropriate solvent. Photoluminescence spectra were obtained on a Horiba Instruments PTI QuantaMaster Series fluorometer. Quartz cuvettes (10 mm x 10 mm or 2 mm x 10 mm or 3 mm x 3 mm, Starna Cells or Thorlabs) were used for absorbance and photoluminescence measurements. All spectra were obtained at ambient temperature. Normalized spectra are displayed for clarity. Absorption coefficient (ε_{max}) values in DCM were calculated using serial dilutions with Hamilton syringes in volumetric glassware and are displayed as the mean ± SD (n = 3 measurements). Relative quantum yields were determined in DCM relative to IR-26 in DCM. See Supplementary Note 3 for a detailed discussion of quantum yield measurements.

General synthetic procedures

Flavones **13a**–**c** were synthesized by subjecting the corresponding 3-aminophenol (150–750 mg scale, 1.0 equiv.) to ethyl benzoylacetate (1.75–2.0 equiv.) and heating at 180 °C for 15–48 h. Compounds were purified by column chromatography with a hexanes/EtOAc solvent gradient (51–55% yield, see Supplementary Table 1). Flavone **15** was synthesized following a known procedure[62] from 7-hydroxyflavone **16**. Flavones **13d**–**h** were synthesized by subjecting flavone **15** (50–180 mg scale, 1.0 equiv.) to the corresponding secondary amine (1.5–2.8 equiv.), RuPhos Pd G3 (0.1 equiv.), RuPhos (0.1 equiv.), and cesium carbonate (1.5 equiv.), in either toluene (at 100–110 °C) or THF (at 50 °C) (0.1–0.3 M) for 5.5–22 h. Compounds were purified by column chromatography with a hexanes/EtOAc solvent gradient (63–83% yield, see Supplementary Table 2). Flavone **13i** was synthesized by subjecting 7-aminoflavone (**17**) (180 mg scale, 1.0 equiv.) to di-*tert*-butyl dicarbonate (3.2 equiv.), triethylamine (2.5 equiv.), dimethylamino pyridine (0.3 equiv.) in THF (0.2 M), and heating to reflux for 48 h. The compound was purified by column chromatography with a hexanes/EtOAc solvent gradient (66% yield).

Flavyliums **12a**–**i** were synthesized by subjecting the corresponding flavone (**13a**–**i**) (20–770 mg scale, 1.0 equiv.) to methyl magnesium bromide (1.5–3.2 equiv.) in THF (0.05–0.1 M), at 0 °C, warming to r.t. and stirring for 12–24 h. The reaction was quenched with aq. fluoroboric acid, extracted with DCM/aq. fluoroboric acid, dried, and filtered. The compounds were purified by trituration with EtOAc, or with diethyl ether/toluene (39–86 % yield, **12i** not isolated for yield, see Supplementary Table 3). Flavylium **12j** was synthesized following a literature procedure[45].

Heptamethine dyes **1**–**11** were synthesized by subjecting the corresponding flavylium (**12a**–**j**) (10–150 mg scale, 1.0 equiv.) to *N*-[(3-(anilinomethylene)-2-chloro-1-cyclohexen-1-yl)methylene]aniline hydrochloride (**18**) (0.40–0.49 equiv.) with either sodium acetate or 2,6-di-*tert*-butyl-4-methylpyridine (1.5–5.6 equiv.) in either *n*-butanol/toluene, 1,4-dioxane, ethanol, or *n*-pentanol (0.05–0.1 M) at 70–140 °C, for 10–120 min. Compounds were purified by a mixture of column chromatography (with a gradient of either DCM/EtOH, DCM/acetone, DCM/MeCN, or DCM/toluene/EtOH), trituration (in toluene, THF), and Soxhlet extraction (compound **10**, in toluene) (5–51% yield, see Supplementary Table 4). See synthetic procedures and characterization in the Supplementary Information for individual procedures used to obtain each flavone, flavylium, and heptamethine dye and full characterization of all novel compounds.

Animal procedures

Animal experiments were conducted in conformity with the institutional guidelines. Non-invasive whole mouse imaging was performed on athymic nude female mice (6–16 weeks old, weight between 20–25 g), purchased from Envigo. Mice were anesthetized with an i.p. injection of a ketamine/xylazine mixture. Tail vein injections were performed with a catheter assembled from a 30-gauge needle connected through plastic tubing to a syringe prefilled with isotonic saline solution. The bevel of the needle was then inserted into the tail vein and secured using tissue adhesive. The plastic tubing was then connected to a syringe (30-gauge

needle) prefilled with the probe of interest. All probes were filtered through a 0.22 μm syringe filter prior to i.v. injection.

SWIR imaging apparatus

For whole mouse imaging, a custom-built setup was used. Lumics laser units: LU1064DLD350-S70AN03 (35 W) “1064 nm”; LU0980D350-D30AN (35W) “980 nm”, and LU0785DLU250-S70AN03 (25 W) “785 nm” were used for excitation. Laser modules are specced to ± 10 nm. Laser outputs were coupled in a 4 × 1 fan-out fiber-optic bundle (Thorlabs BF46LS01) of 600 μm core diameter for each optical path. The output from the fiber was fixed in an excitation cube (Thorlabs KCB1EC/M), reflected off of a mirror (Thorlabs BBE1-E03), and passed through a positive achromat (Thorlabs AC254–050-B), SP filter (if necessary) and a ground glass diffuser (Thorlabs DG10–120-MD) or an engineered diffuser (Thorlabs ED1-S20-MD) to provide uniform illumination over the working area. In a typical experiment, the excitation flux at the object was adjusted to be close to 100 $mWcm^{-2}$ with an error of ± 3% (power density used is defined separately in each experiment). The working area was covered by a heating mat coated with blackout fabric (Thorlabs BK5). Emitted light was directed onto an Allied Vision Goldeye G-032 Cool TEC2 camera with a sensor temperature set point of −20 °C.

Two lens systems were used, as follows:

Lens system A: Emitted light was directed through a 4-inch square first-surface silver mirror (Edmund Optics, 84448) with a custom filter set (defined for each experiment) and a C-mount camera lens (Navitar, SWIR-35).

Lens system B: The custom lens system consists of a 4f configuration with three f = 500.0 mm lenses (Thorlabs LB1909-C) and two f = 200.0 mm lenses (Thorlabs LB1199-C) with a custom filter set (defined for each experiment). For ergonomic reasons, a 2” protected silver-coated elliptical mirror (PFE20-P01) mounted to a kinematic mount (Thorlabs KCB2EC/M) was used.

The assembly was partially enclosed to avoid excess light while enabling manipulation of the field of view during operation. The image acquisition toolbox of MATLAB programming environment was used in combination with a custom MATLAB script to preview and collect the required image data in 8-bit or 12-bit format. The prepared MATLAB script allows users to access basic functionalities of the image acquisition device by establishing a packet jitter free data streaming link between the desktop computer and the acquisition device.

Multiplexed imaging acquisition:

To facilitate real-time multiplexed imaging, a programmable trigger controller (Atmel Atmega328 micro-controller unit) implemented with an Arduino Nano Rev 3 MCU (A000005) micro-controller unit is used to deliver sequential trigger pulses of 5V Transistor–Transistor Logic to the laser driver units and InGaAs camera. Predetermined triggering sequences written in the Arduino Integrated Development Environment are uploaded from a PC via USB interface to the micro-controller unit. A semi-automatic

imaging algorithm adopted in MATLAB (see above, SWIR imaging apparatus), in combination with manual control of laser parameters via the individual laser modules, and the programmed micro-controller unit facilitate excitation-synchronized imaging. Excitation-synchronized frames are collected by the camera, and transferred to the PC via GigE interface. Further information and illustrative figures can be found in Supplementary Note 5.

Image processing procedures:

Images were processed using the Fiji distribution[63] of ImageJ.[64] All images were background corrected with a 10-frame averaged background file to correct for non-linearities in the detector and/or excitation. Raw images underwent no further processing. Unmixed images were image subtracted according to the relative contribution of each channel, determined separately for each experiment, and detailed in the Supplementary Information, in the figure experimental procedures. All still images were averaged over 5 frames and converted to 8-bit PNG files for display, unless stated otherwise. Videos were frame averaged to reduce file size, if necessary, before compression with FFmpeg to a .mov file.

Additional methods information included in the Supplementary Information file includes experimental procedures specific to each figure, supplementary figure and supplementary video, supplementary notes which contain synthetic discussion, Hammett plot calculations, SWIR imaging with triggered excitation multiplexing, and the photoluminescence quantum yields, and the synthetic procedures and characterization.

Extended Data

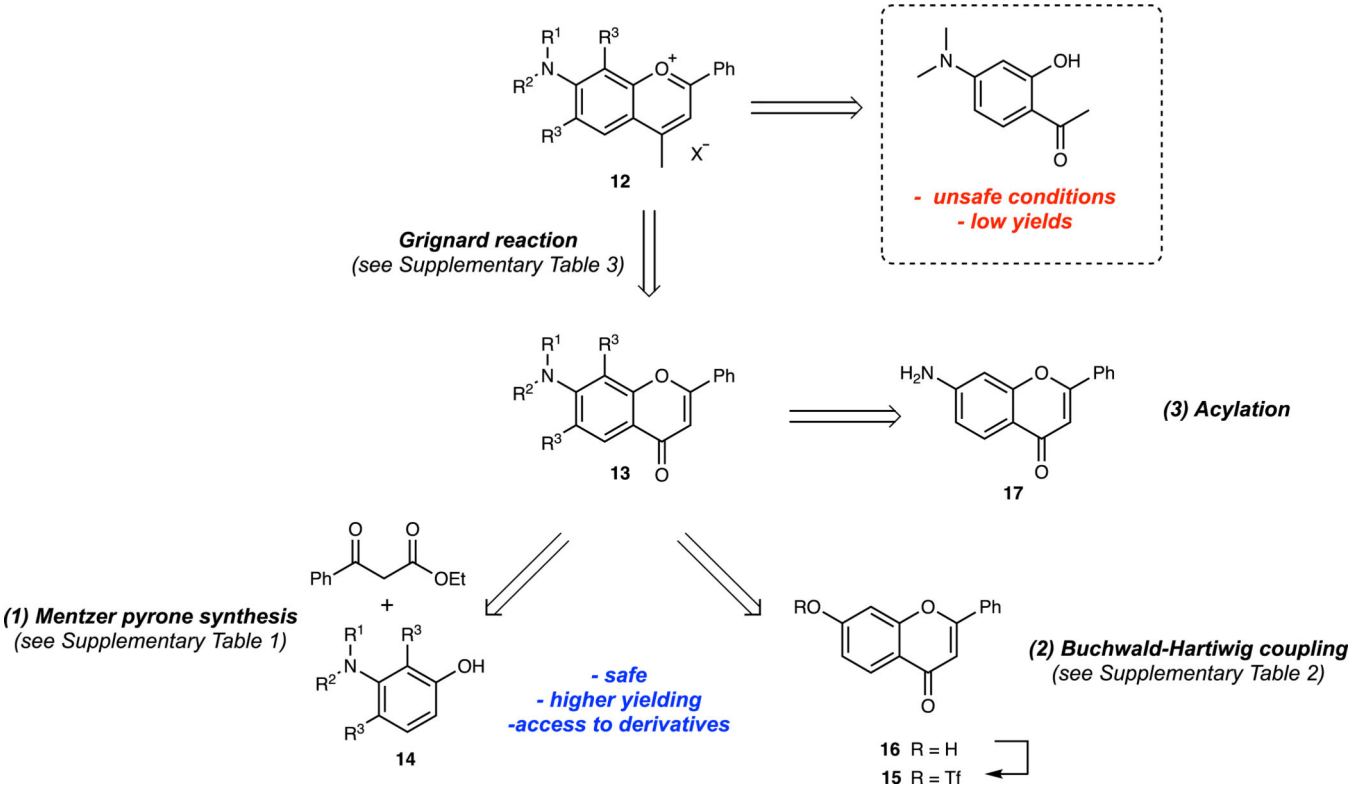

Extended Data Fig. 1.
Retrosynthesis of 7-aminoflavylium heterocycles.

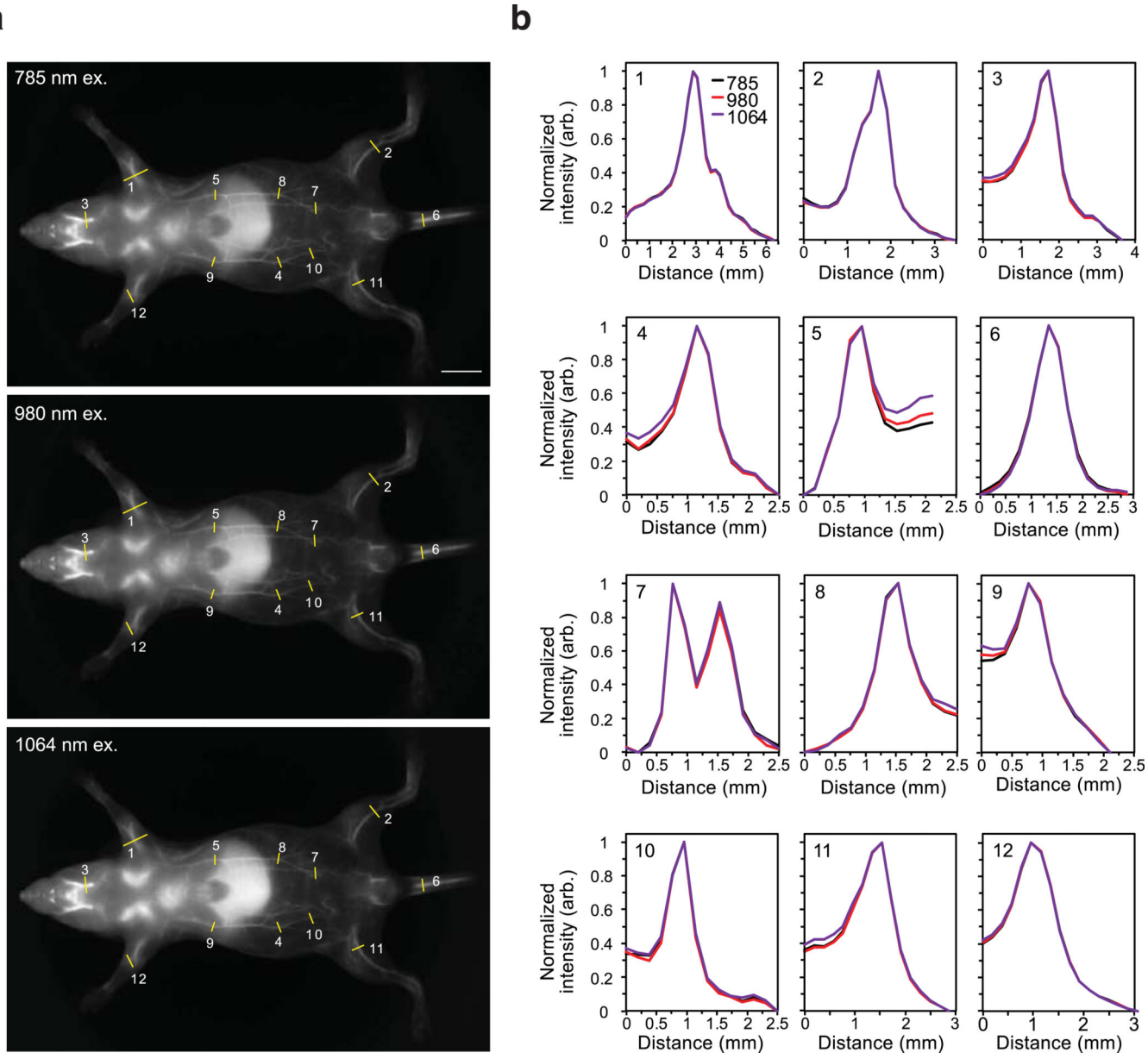

Extended Data Fig. 2. Resolution effects upon excitation multiplexing and single-channel detection in the SWIR.

a) Images of a mouse phantom acquired after injection of JuloFlav7 (**3**) (94 nmol) and immediate sacrifice. Images were acquired with 785 nm ex. (93 $mWcm^{-2}$), 980 nm (30 $mWcm^{-2}$), and 1064 nm (11 $mWcm^{-2}$) and collection 1150–1700 nm (48 ms, 20 fps). Displayed images are averaged over 200 frames. b) To observe resolution, 12 cross-sections were drawn over different vessels (labelled in a) and the baseline subtracted and normalized cross-sections are overlaid.

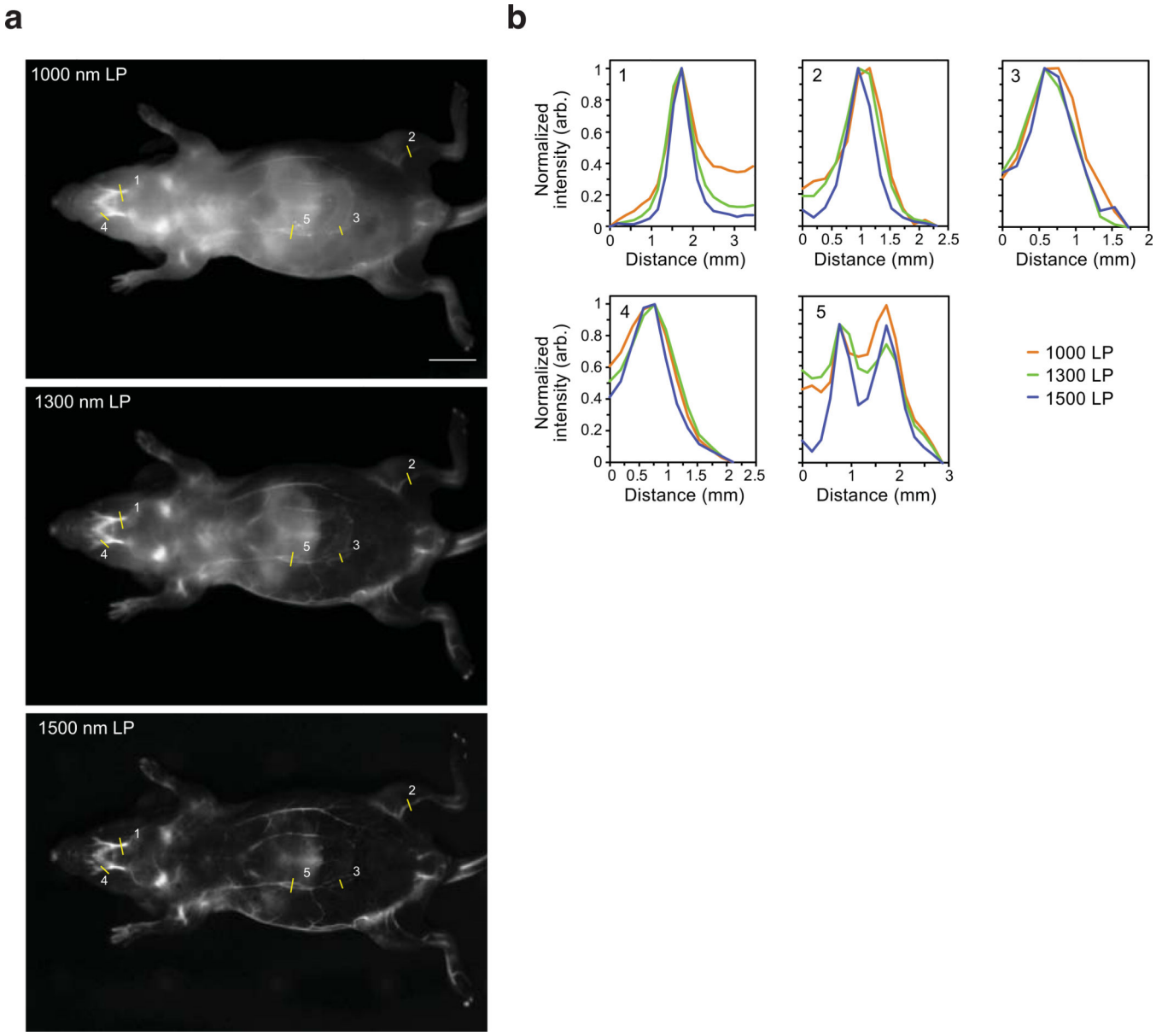

Extended Data Fig. 3. Resolution effects observed upon emission multiplexing with a single excitation wavelength in the SWIR.

a) Images of a mouse phantom acquired after injection of JuloFlav7 (**3**) (94 nmol) and immediate sacrifice, after one freeze-thaw cycle. Images were acquired with 980 nm ex. Laser powers and exposure time are as follows (1) 1000 nm LP = 8.1 $mWcm^{-2}$, 30 ms; 1300 nm LP = 24 $mWcm^{-2}$, 500 ms; 1500 nm LP = 177 $mWcm^{-2}$, 500 ms. Displayed images are averaged over 200 frames. b) To observe resolution, 5 cross-sections were drawn over different vessels (labelled in a) and the baseline subtracted and normalized cross-sections are overlaid.

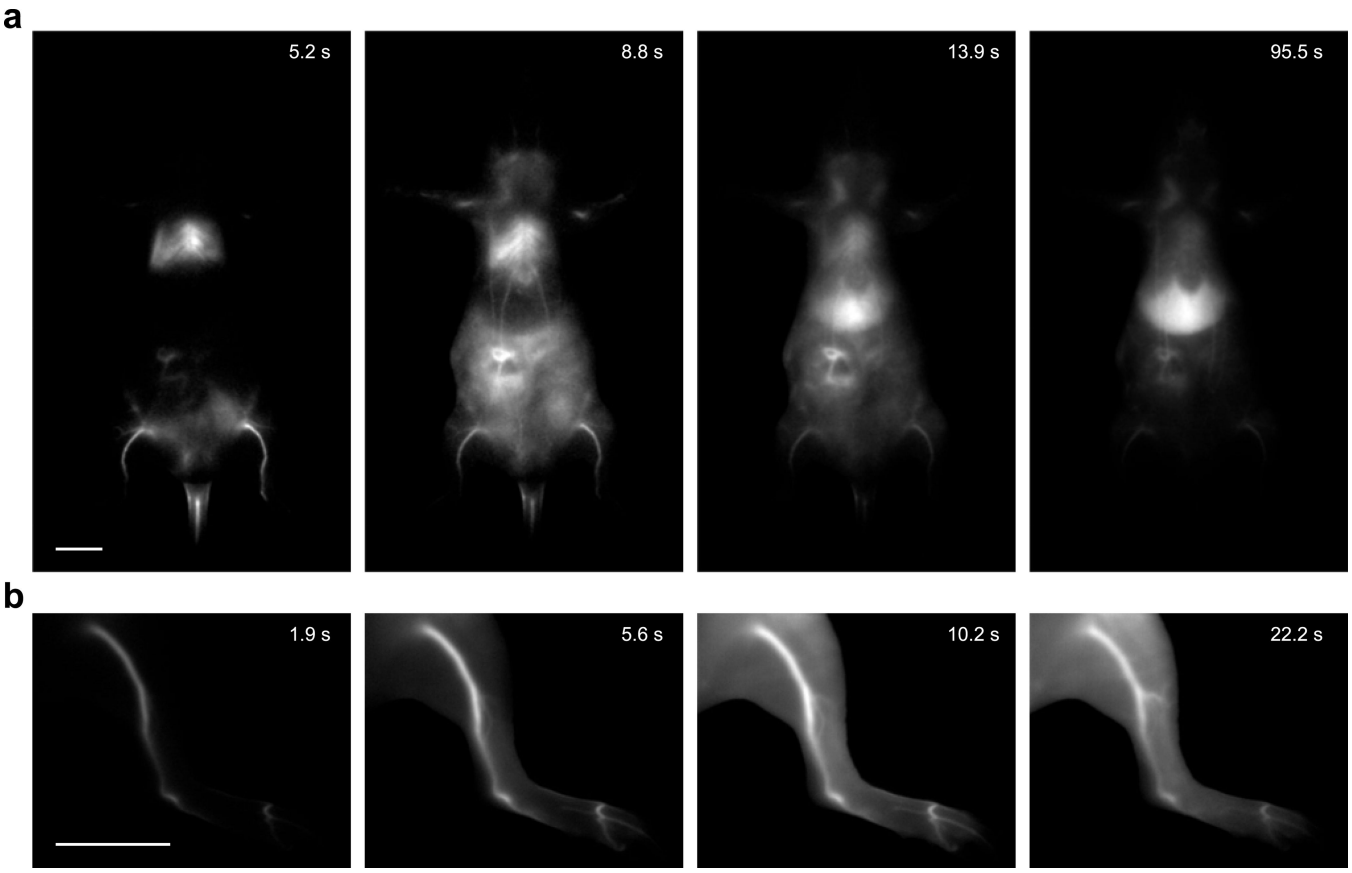

Extended Data Fig. 4. Imaging with 1064 nm excitation after injection of JuloFlav7 (3) micelles.
a) Whole mouse imaging at selected time-points after i.v. injection of JuloFlav7 micelles (44 nmol) in PBS buffer with excitation at 1064 nm (103 $mWcm^{-1}$) and 1150–1700 nm collection (8 ms exposure time, 100 fps). b) Imaging of the mouse hind-limb at selected time points after i.v. injection of JuloFlav7 micelles (55 nmol) with excitation at 1064 nm (95 $mWcm^{-1}$) with 1100–1700 nm collection (9 ms exposure time, 100 fps). Displayed images are averaged over 5 frames. Scale bars represent 1 cm. Data are representative of two replicate experiments.

Supplementary Material

Refer to Web version on PubMed Central for supplementary material.

Acknowledgements

This work was supported by grants to E.D.C. (NSF GRFP DGE-1144087, Christopher S. Foote Fellowship), O.T.B. (Emmy-Noether-Programme of DFG BR 5355/2–1, Helmholtz Pioneer Campus Institute for Biomedical Engineering), E.M.S. (UCLA, Sloan Research Award FG-2018–10855, NIH 1R01EB027172–01), Helmholtz Zentrum München, and by shared instrumentation grants from the NSF (CHE-1048804) and NIH (1S10OD016387–01). We thank Thomas Schwarz-Romond, Thomas S. Bischof, Doris Bengel, Kendall N. Houk, Justin R. Caram, and Luke D. Lavis for discussions and support and the Garcia-Garibay Group for instrumentation. Correspondence and requests for materials should be addressed to E.M.S and O.T.B.

References

1. Dean KM & Palmer AE Advances in fluorescence labeling strategies for dynamic cellular imaging. Nat. Chem. Biol. 10, 512–523 (2014). [PubMed: 24937069]
2. Wei L. et al. Super-multiplex vibrational imaging. Nature 544, 465–470 (2017). [PubMed: 28424513]
3. Frangioni JV *In vivo* near-infrared fluorescence imaging. Curr. Opin. Chem. Biol. 7, 626–634 (2003). [PubMed: 14580568]
4. Kong L. et al. Continuous volumetric imaging via an optical phase-locked ultrasound lens. Nat. Methods 12, 759–762 (2015). [PubMed: 26167641]
5. Grimm JB et al. A general method to fine-tune fluorophores for live-cell and *in vivo* imaging. Nat. Methods 14, 987–994 (2017). [PubMed: 28869757]
6. Fenrich KK et al. Long-term *in vivo* imaging of normal and pathological mouse spinal cord with subcellular resolution using implanted glass windows. J. Physiol. 590, 3665–3675 (2012). [PubMed: 22641787]
7. Rakhymzhan A. et al. Synergistic strategy for multicolor two-photon microscopy: application to the analysis of germinal center reactions *in vivo*. Sci. Rep. 7, 7101 (2017). [PubMed: 28769068]
8. Kim P, Puoris'haag M, Côté D, Lin CP & Yun SH *In vivo* confocal and multiphoton microendoscopy. J. Biomed. Opt. 13, 010501 (2008).
9. Kosaka N, Ogawa M, Sato N, Choyke PL & Kobayashi H. *In vivo* real-time, multicolor, quantum dot lymphatic imaging. J. Invest. Dermatol. 129, 2818–2822 (2009). [PubMed: 19536144]
10. Erogbogbo F. et al. In vivo targeted cancer imaging, sentinel lymph node mapping and multi-channel imaging with biocompatible silicon nanocrystals. ACS Nano 5, 413–423 (2011). [PubMed: 21138323]
11. Shcherbakova DM & Verkhusha VV Near-infrared fluorescent proteins for multicolor *in vivo* imaging. Nat. Methods 10, 751–754 (2013). [PubMed: 23770755]
12. Zavaleta CL et al. Multiplexed imaging of surface enhanced Raman scattering nanotags in living mice using noninvasive Raman spectroscopy. Proc. Natl. Acad. Sci. USA 106, 13511–13516 (2009).
13. Zhang H. et al. Penetration depth of photons in biological tissues from hyperspectral imaging in shortwave infrared in transmission and reflection geometries. J. Biomed. Opt. 21, 126006 (2016).
14. Carr JA et al. Absorption by water increases fluorescence image contrast of biological tissue in the shortwave infrared. Proc. Natl. Acad. Sci. USA 115, 9080–9085 (2018). [PubMed: 30150372]
15. Naczynski DJ et al. Rare-earth-doped biological composites as *in vivo* shortwave infrared reporters. Nat. Commun. 4, 2199 (2013). [PubMed: 23873342]
16. Welsher K. et al. A route to brightly fluorescent carbon nanotubes for near-infrared imaging in mice. Nat. Nanotechnol. 4, 773–780 (2009). [PubMed: 19893526]
17. Hong G. et al. In vivo fluorescence imaging with Ag2S quantum dots in the second near-infrared region. Angew. Chemie Int. Ed. 51, 9818–9821 (2012).
18. Bruns OT et al. Next-generation *in vivo* optical imaging with short-wave infrared quantum dots. Nat. Biomed. Eng. 1, 0056 (2017).
19. Tao Z. et al. Biological imaging using nanoparticles of small organic molecules with fluorescence emission at wavelengths longer than 1000 nm. Angew. Chemie Int. Ed. 52, 13002–13006 (2013).
20. Yang Q. et al. Rational design of molecular fluorophores for biological imaging in the NIR-II window. Adv. Mater. 29, 1605497 (2017).
21. Zhu S. et al. 3D NIR-II molecular imaging distinguishes targeted organs with high-performance NIR-II bioconjugates. Adv. Mater. 30, 1705799 (2018).
22. Wan H. et al. A bright organic NIR-II nanofluorophore for three-dimensional imaging into biological tissues. Nat. Commun. 9, 1171 (2018). [PubMed: 29563581]
23. Wang F. et al. Light-sheet microscopy in the near-infrared II window. Nat. Methods 16, 545–552 (2019). [PubMed: 31086342]

24. Zhu S. et al. Molecular imaging of biological systems with a clickable dye in the broad 800- to 1,700-nm near-infrared window. Proc. Natl. Acad. Sci. USA 114, 962–967 (2017). [PubMed: 28096386]
25. Ma BL, Zhai X, Du G. & Zhou J. Orthogonal shortwave infrared emission based on rare earth nanoparticles for interference-free logical codes and bio-imaging. Chem. Sci. 10, 3281–3288 (2019). [PubMed: 30996913]
26. Hong G. et al. Through-skull fluorescence imaging of the brain in a new near-infrared window. Nat. Photonics 8, 723–730 (2014). [PubMed: 27642366]
27. Diao S. et al. Fluorescence imaging in vivo at wavelengths beyond 1500 nm. Angew. Chemie Int. Ed. 54, 14758–14762 (2015).
28. Kapanidis AN et al. Alternating-laser excitation of single molecules. Acc. Chem. Res. 38, 523–533 (2005). [PubMed: 16028886]
29. Müller BK, Zaychikov E, Bräuchle C. & Lamb DC Pulsed interleaved excitation. Biophys. J. 89, 3508–3522 (2005). [PubMed: 16113120]
30. Lewis EK et al. Color-blind fluorescence detection for four-color DNA sequencing. Proc. Natl. Acad. Sci. USA 102, 5346–5351 (2005). [PubMed: 15800037]
31. Garbacik ET, Sanz-Paz M, Borgman KJE, Campelo F. & Garcia-Parajo MF Frequency-Encoded Multicolor Fluorescence Imaging with Single-Photon-Counting Color-Blind Detection. Biophys. J. 115, 725–736 (2018). [PubMed: 30037496]
32. Gómez-García PA, Garbacik ET, Otterstrom JJ, Garcia-Parajo MF & Lakadamyali M. Excitation-multiplexed multicolor superresolution imaging with fm-STORM and fm-DNA-PAINT. Proc. Natl. Acad. Sci. USA 115, 12991–12996 (2018). [PubMed: 30509979]
33. Thimsen E, Sadtler B. & Berezin MY Shortwave-infrared (SWIR) emitters for biological imaging: a review of challenges and opportunities. Nanophotonics 6, 1043–1054 (2017).
34. Bricks JL, Kachkovskii AD, Slominskii YL, Gerasov AO & Popov SV Molecular design of near infrared polymethine dyes: A review. Dyes Pigm. 121, 238–255 (2015).
35. Marshall MV et al. Near-infrared fluorescence imaging in humans with indocyanine green: a review and update. Open Surg. Oncol. J. 2, 12–25 (2010). [PubMed: 22924087]
36. Rurack K. & Spieles M. Fluorescence quantum yields of a series of red and near-infrared dyes emitting at 600−1000 nm. Anal. Chem. 83, 1232–1242 (2011). [PubMed: 21250654]
37. Carr JA et al. Shortwave infrared fluorescence imaging with the clinically approved near-infrared dye indocyanine green. Proc. Natl. Acad. Sci. USA 115, 4465–4470 (2018).; Preprint at 10.1101/100768v1 (2017). [PubMed: 29626132]
38. Starosolski Z. et al. Indocyanine green fluorescence in second near-infrared (NIR-II) window. PLoS One 12, e0187563 (2017).
39. Cosco ED et al. Flavylium polymethine fluorophores for near- and shortwave infrared imaging. Angew. Chem. Int. Ed. 56, 13126–13129 (2017).
40. Henary M, Mojzych M, Say M. & Strekowski L. Functionalization of benzo[*c,d*]indole system for the synthesis of visible and near-infrared dyes. J. Heterocycl. Chem. 46, 84–87 (2009).
41. Li B, Lu L, Zhao M, Lei Z. & Zhang F. An efficient 1064 nm NIR-II excitation fluorescent molecular dye for deep-tissue high-resolution dynamic bioimaging. Angew. Chem. Int. Ed. 57, 7483–7487 (2018).
42. Ding B. et al. Polymethine thiopyrylium fluorophores with absorption beyond 1000 nm for biological imaging in the second near-infrared subwindow. J. Med. Chem. 62, 2049–2059 (2019). [PubMed: 30501190]
43. Wang S. et al. Anti-quenching NIR-II molecular fluorophores for *in vivo* high-contrast imaging and pH sensing. Nat. Commun. 10, 1058 (2019). [PubMed: 30837470]
44. Lei Z. et al. Stable, wavelength-tunable fluorescent dyes in the NIR-II region for *in vivo* high-contrast bioimaging and multiplexed biosensing. Angew. Chemie Int. Ed. 58, 8166–8171 (2019).
45. Chen J-R, Wong J-B, Kuo P-Y & Yang D-Y Synthesis and characterization of coumarin-based spiropyran photochromic colorants. Org. Lett. 10, 4823–4826 (2008). [PubMed: 18826232]

46. Roehri-stoeckel C, Gonzalez E. & Fougerousse A. Synthetic dyes: simple and original ways to 4-substituted flavylium salts and their corresponding vitisin derivatives. Can J. Chem. 79, 1173–1178 (2001).
47. Seijas JA, Vázquez-Tato MP & Carballido-Reboredo R. Solvent-free synthesis of functionalized flavones under microwave irradiation. J. Org. Chem. 70, 2855–2858 (2005). [PubMed: 15787587]
48. Kónya K, Pajtás D, Kiss-Szikszai A. & Patonay T. Buchwald-Hartwig reactions of monohaloflavones. Eur. J. Org. Chem. 2015, 828–839 (2015).
49. Kopainsky B, Qiu P, Kaiser W, Sens B. & Drexhage KH Lifetime, photostability, and chemical structure of IR heptamethine cyanine dyes absorbing beyond 1 μm. Appl. Phys. B 29, 15–18 (1982).
50. Hansch C, Leo A. & Taft RW A survey of Hammett substituent constants and resonance and field parameters. Chem. Rev. 91, 165–195 (1991).
51. Semonin OE et al. Absolute photoluminescence quantum yields of IR-26 Dye, PbS, and PbSe quantum dots. J. Phys. Chem. Lett 1, 2445–2450 (2010).
52. Hatami S. et al. Absolute photoluminescence quantum yields of IR26 and IR-emissive Cd1−xHgxTe and PbS quantum dots – method- and material-inherent challenges. Nanoscale 7, 133–143 (2015). [PubMed: 25407424]
53. Lukasik VM & Gillies RJ Animal anaesthesia for *in vivo* magnetic resonance. NMR Biomed. 16, 459–467 (2003). [PubMed: 14696002]
54. Schwenke DO, Pearson JT, Mori H. & Shirai M. Long-term monitoring of pulmonary arterial pressure in conscious, unrestrained mice. J. Pharmacol. Toxicol. Methods 53, 277–283 (2006). [PubMed: 16338149]
55. Sato M. et al. Simultaneous monitoring of mouse respiratory and cardiac rates through a single precordial electrode. J. Pharmacol. Sci. 137, 177–186 (2018). [PubMed: 30042023]
56. Ceppi L. et al. Real-time single-walled carbon nanotube-based fluorescence imaging improves survival after debulking surgery in an ovarian cancer model. ACS Nano 13, 5356–5365 (2019). [PubMed: 31009198]
57. Zhu S, Tian R, Antaris AL, Chen X. & Dai H. Near-infrared-II molecular dyes for cancer imaging and surgery. Adv. Mater. e1900321 (2019).
58. Cousins A, Thompson SK, Wedding AB & Thierry B. Clinical relevance of novel imaging technologies for sentinel lymph node identification and staging. Biotechnol. Adv. 32, 269–279 (2014). [PubMed: 24189095]
59. Rasmussen JC, Fife CE & Sevick-Muraca EM Near-infrared fluorescence lymphatic imaging in lymphangiomatosis. Lymphat. Res. Biol. 13, 195–201 (2015). [PubMed: 26287470]
60. Tozzi M, Boni L, Soldini G, Franchin M. & Piffaretti G. Vascular fluorescence imaging control for complex renal artery aneurysm repair using laparoscopic nephrectomy and autotransplantation. Case Rep. Transplant. 2014, 563408 (2014).

References (for methods):

61. Bexrud JA, Eisenberger P, Leitch DC, Payne PR & Schafer LL Selective C-H activation α to primary amines. Bridging metallaaziridines for catalytic, intramolecular α-alkylation. J. Am. Chem. Soc. 131, 2116–2118 (2009). [PubMed: 19173650]
62. Kövér J. & Antus S. Facile Deoxygenation of hydroxylated flavonoids by palladium-catalysed reduction of its triflate derivatives. Z. Naturforsch. 60b, 792–796 (2005).
63. Schindelin J. et al. Fiji: an open-source platform for biological-image analysis. Nat. Methods 9, 676–682 (2012). [PubMed: 22743772]
64. Rueden CT et al. ImageJ2: ImageJ for the next generation of scientific image data. BMC Bioinformatics 18, 529 (2017). [PubMed: 29187165]

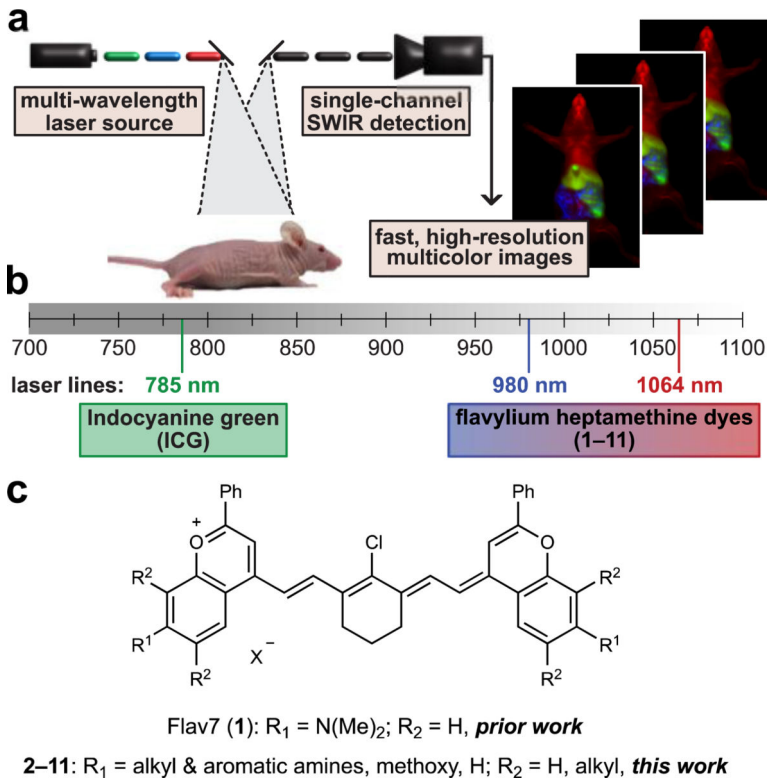

Fig. 1.

Real-time excitation-multiplexed SWIR imaging design. a) Multiple laser sources are pulsed and delivered to the biological sample. Single-channel SWIR detection (InGaAs, 1150–1700 nm) acquires frames which are temporally separated by color on the ms time scale. Fast frame rates produce real-time multicolor *in vivo* images at up to 50 frames per second (fps). b) Relevant portions of the NIR and SWIR regions of the electromagnetic spectrum, lasers used for excitation, and dyes used and/or presented in this study which are excited by the distinct laser lines. c) Flavylium polymethine scaffold explored here to match bright SWIR dyes to appropriate lasers.

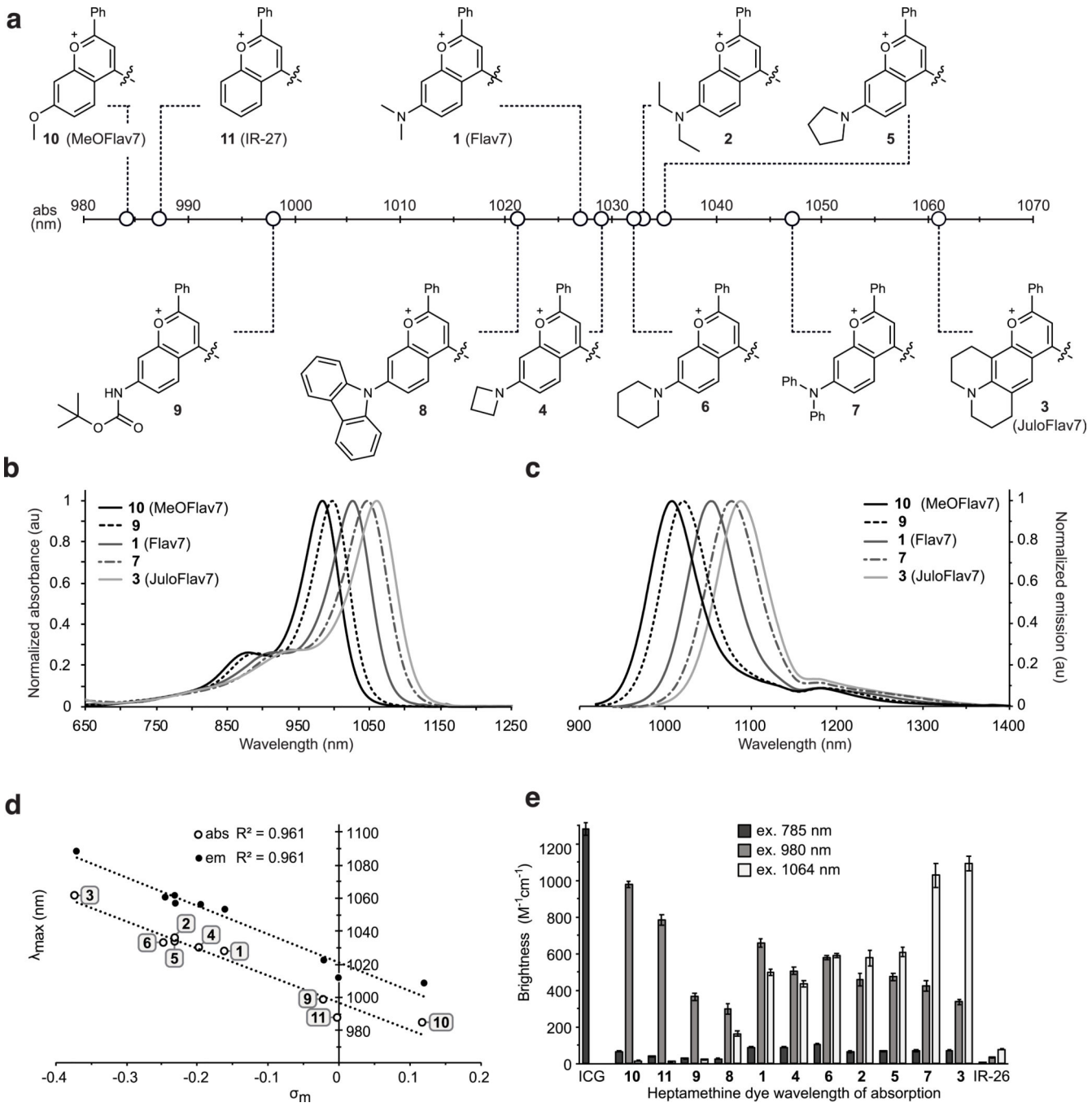

Fig. 2.

Panel of flavylium heptamethine dyes and their photophysical properties. a) Heterocycle structures and absorption wavelength maxima visualized graphically on the electromagnetic spectrum. b) Absorption and c) Emission profiles (ex. 885 nm) of selected polymethine dyes. d) Hammett plot relating σ_m substituent constants (ref. 50) to absorption and emission wavelengths of dyes 1–6 and 9–11. e) Brightness (defined as $\epsilon_\lambda \times \Phi_F$) of the heptamethine derivatives at relevant excitation wavelengths (λ = 785 nm (dark grey), λ = 980 nm (light

grey), and λ = 1064 nm (white). Error bars represent the propagated error from standard deviations in ϵ and $\mathbf{\Phi_F}$ measurements.

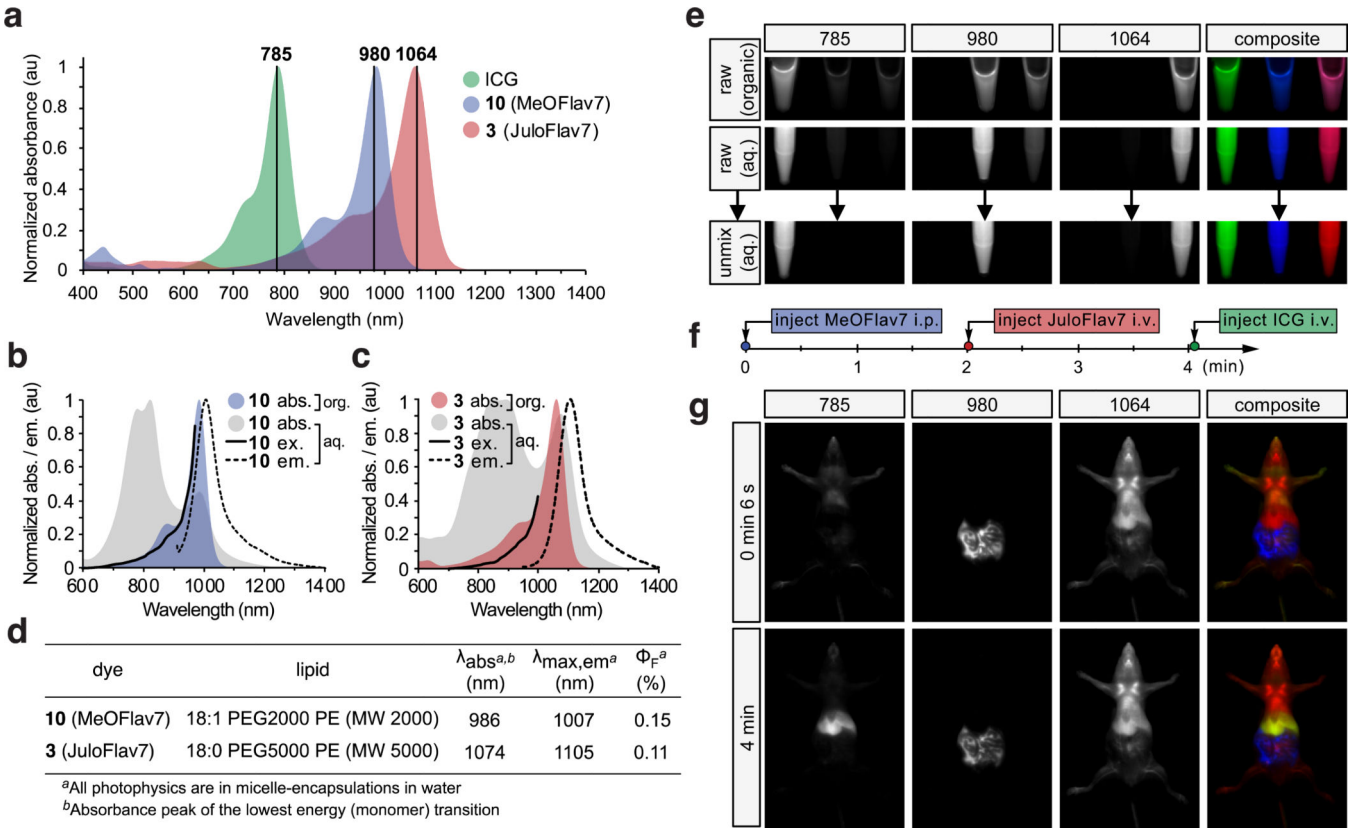

dye	lipid	$\lambda_{abs}{}^{a,b}$ (nm)	$\lambda_{max,em}{}^{a}$ (nm)	$\Phi_F{}^{a}$ (%)
10 (MeOFlav7)	18:1 PEG2000 PE (MW 2000)	986	1007	0.15
3 (JuloFlav7)	18:0 PEG5000 PE (MW 5000)	1074	1105	0.11

[a]All photophysics are in micelle-encapsulations in water
[b]Absorbance peak of the lowest energy (monomer) transition

Fig. 3.

Excitation-multiplexed SWIR imaging. a) Absorption profiles of dyes used in imaging experiments plotted against excitation wavelengths employed. b-c) Absorption (grey), emission (ex. at 880 nm (b) and 900 nm (c), black dotted), and excitation spectra (em. monitored at 1008 nm (b), and 1088 nm (c), black solid) of micelle-encapsulated 10 (b) and 3 (c) overlaid with absorption traces of dyes in DCM (colored). d) Photophysics of the micelle-encapsulated dyes in water. e) Raw and unmixed images of successive frames and merged 3-color images of vials containing ICG (left), 10 (center), and 3 (right) in ethanol or DCM (top) and in micelles in water (middle and bottom). Arrow indicates linear unmixing procedure. f) Experimental timeline of administration of the three probes used in (g). g) Multiplexed *in vivo* images using 785, 980, and 1064 nm ex. (78 $mWcm^{-2}$) and 1150–1700 nm collection (10 ms exposure time; 27.8 fps). Displayed images are averaged over 5 frames.

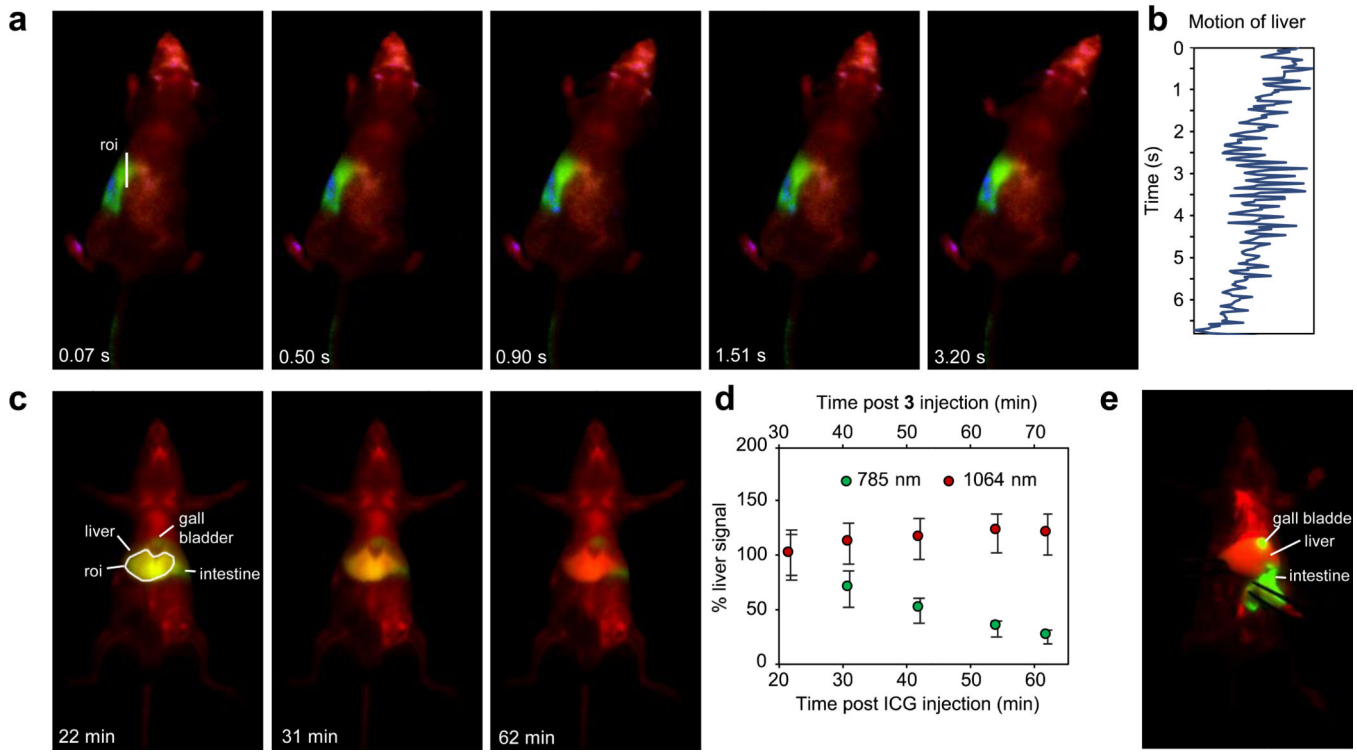

Fig. 4.

Applications enhanced by SWIR multiplexed imaging. a) Multiplexed imaging of an awake mouse showing one continuous movement of the head with 785, 980, and 1064 nm ex. (78 $mWcm^{-2}$) and 1150–1700 nm collection (10 ms exposure time; 27.8 fps). Displayed images are a single frame. b) Awake breathing rate (247 breaths per minute), analyzed by quantifying the liver motion (by the center of mass) over the region of interest (roi) in (a). c) Imaging of ICG clearance with systemic labelling by 3 micelles. Multiplexed *in vivo* images using 785 and 1064 nm ex. (100 $mWcm^{-2}$) and 1150–1700 nm collection (5 ms exposure time; 50 fps). Displayed images are averaged over 5 frames. d) Percent signal in the liver of ICG and micelles of 3 over one hour. Data are displayed as the mean intensity over the roi (in c) ± SD, n = 805 pixels. e) Two-color necropsy procedure, captured in real-time in Supplementary Video 5. Acquisition settings are as in (c).

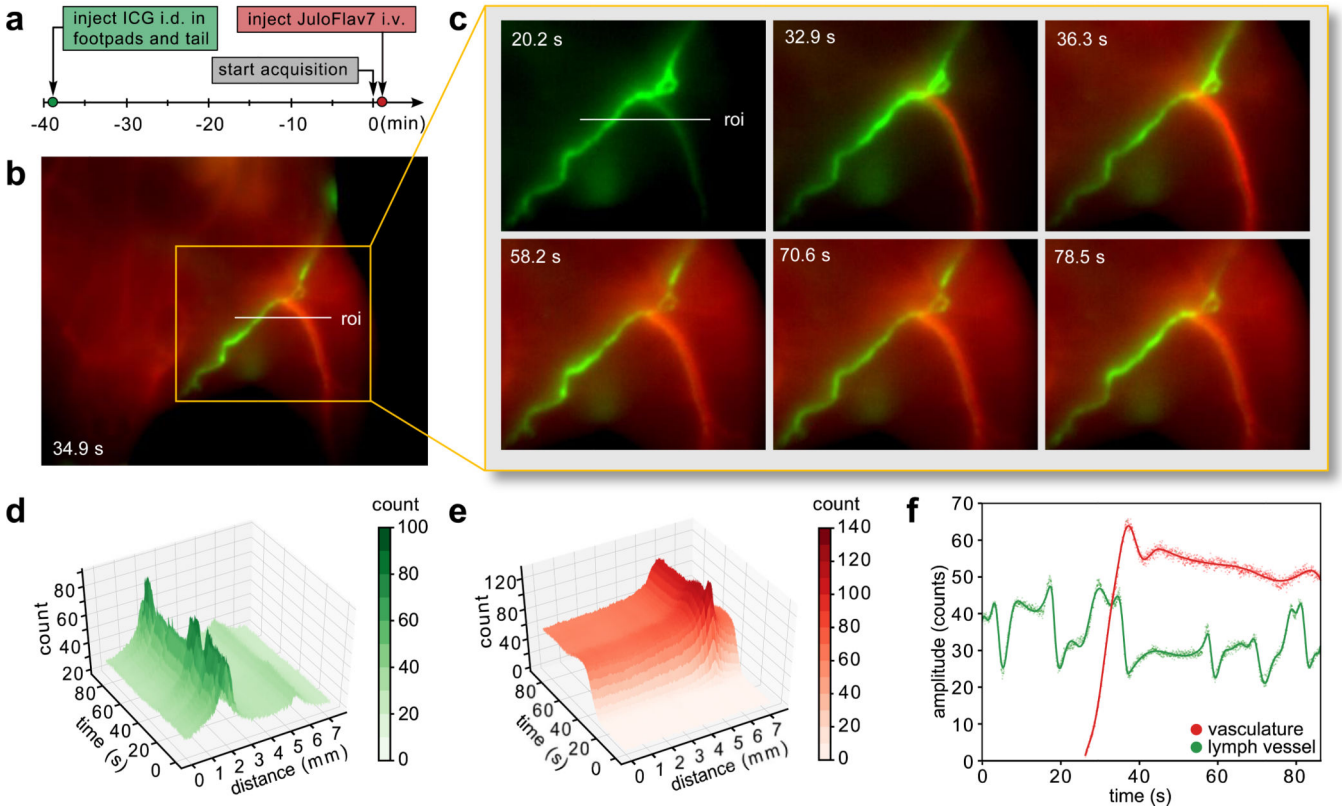

Fig. 5.

Orthogonal lymphatic and circulatory imaging with high spatiotemporal resolution after intradermal (i.d.) injection of ICG and intravenous (i.v.) injection of 3 micelles. a) Experimental timeline. b) Representative image acquired 30 s after injection of 3 micelles. c) Time points over the relevant time period analyzed in (d–f). d-e) 3D plots of the 785 nm channel (d) and 1064 nm channel (e) demonstrating simultaneous intensity information in two colors over the roi indicated in (b) and (c), and highlighting the spatial and temporal resolution captured. Contour plots are shown in Supplementary Fig. 9. f) The signal in each vessel over time can be quantified by plotting the amplitude of the vessel, fit as a gaussian curve at each frame (points). The data is interpolated using a smoothing spline fit (solid lines). Acquisition: 785 and 1064 nm ex. (100 mWcm^{-2}) and 1100–1700 nm collection (20 ms exposure time; 21.7 fps). Displayed images are averaged over 5 frames.

Table 1.

Photophysics of heptamethine fluorophores in DCM

dye	$\lambda_{max,abs}$ (nm)	ε_{max} ($M^{-1}cm^{-1}$)[a]	$\lambda_{max,em}$	Φ_F, (%)[a]	brightness(ε_{max}) ($M^{-1}cm^{-1}$)[a]
1 (Flav7)	1027	241,000	1053	0.61	1,470
2	1033	190,000	1057	0.62	1,180
3 (JuloFlav7)	1061	238,000	1088	0.46	1,090
4	1029	207,000	1056	0.51	1,060
5	1034	247,000	1061	0.48	1,190
6	1032	110,000	1060	0.54	590
7	1047	210,000	1078	0.58	1,220
8	1021	140,000	1048	0.45	630
9	998	108,000	1022	0.42	450
10 (MeOFlav7)	984	190,000	1008	0.52	990
11 (IR-27)	987	231,000	1011	0.35	810
ICG	787[b]	194,000[b]	818[b]	0.66[b,c]	1,200[c]
IR-26	1080	171,000	1114	0.05[d]	86

[a] see Supplementary Fig. 5 for errors in ε_{max} and Φ_F, and brightness(ε_{max})

[b] data taken from ref. 36 (EtOH)

[c] value includes on the % emission between 1000–1300 nm (5%, ref. 37)

[d] value from ref. 51 (DCE), treated as a constant or relative Φ_F, measurements